Multiobjective Optimization Considering PET's Vibration Suppression of Dual Active Bridge Converter Based on BP-NSGA-II

Dong Jiang, *Senior Member, IEEE*, Shang Gong, *Student Member, IEEE*, Zicheng Liu, *Senior Member, IEEE*, Pengye Wang, *Graduate Student Member, IEEE*, Xiaokang Peng, *Student Member, IEEE*, Rui Li, Jiuqing Cai, and Ronghai Qu, *Fellow, IEEE*

***Abstract*—The article proposes a multiobjective optimization procedure for a dual active bridge (DAB) converter based on nondominated sorting genetic algorithm with back propagation (BP) neural network embedded in back propagation nondominated sorting genetic algorithm (BP-NSGA-II), where the BP neural network was used to predict the vibration of power electronic transformer (PET). Experimental results demonstrate the high accuracy of this neural network in vibration fitting of PET. Based on the offline trained neural network, the phase-shift angles corresponding to minimum vibration is found in the triple phase-shift mode of DAB. Compared with common phase-shift modes at the same transmission power level, the optimized method could effectively reduce the vibration amplitude of PET at the key frequency with more than 20 dB. Meanwhile, the vibration amplitude at the concerned frequency of the optimized method is smaller than that of all the training sets. Furthermore, in BP-NSGA-II, the current stress, reflow power, and vibration of PET are used as objective functions to optimize the operating state of DAB further. The experimental results show that the proposed multiobjective optimization method, based on BP-NSGA-II, can improve the performance of the DAB converter by reducing its current stress and reflow power while suppressing the vibration amplitude of PET.**

***Index Terms*—Back propagation (BP) neural network, dual active bridge (DAB), nondominated sorting genetic algorithm (NSGA-II), power electronic transformer (PET), vibration.**

I. INTRODUCTION

IN RECENT years, renewable energy sources such as solar and wind power have received increased attention due to the growing issue of environmental pollution. The advantages of these clean energy sources, including their recyclability and abundant resources, make them an attractive option for energy generation and utilization. Traditional transformers present numerous challenges such as their large size, high energy consumption ratio, and difficult control, which make them unsuitable for the demands of new energy grids [1]. With the development of switching devices, magnetic materials and advanced control methods, power electronic transformers (PETs) with high frequency, high power, and large capacities have been developed and applied to the dual-active-bridge (DAB) dc/dc converter and other areas [2], [3], [4]. PET reduces the volume and weight of the isolated transformer effectively by increasing its working frequency [5], [6]. Compared with the traditional power frequency transformers, PET has higher flexibility and obvious advantages in integrated fault tolerance, power quality regulation, dc access of renewable energy and energy storage equipment, multiport operation, and so on. Hence, it will play a vital role in the future power grid system, electric aircraft and ship power systems and electric vehicle (EV), etc. [7], [8], [9], [10] Fig. 1 represents the typical power electronic transformer power conversion link.

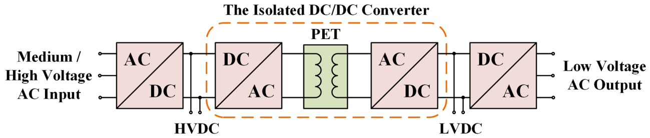

Fig. 1. Typical PET power conversion link.

However, with the increasing demand for power levels of power electronic equipment, the impact of vibration and noise cannot be ignored. On one hand, in the power grid system, the vibration of PET will lead to the wear of the transformer core, loose windings, high local temperature rise, and energy loss. In addition, the vibration is transmitted through the intermediate connecting parts, which can result in structural fatigue and insulation damage of fasteners such as bolts, affecting the normal operation and the service life of the equipment, and reducing the operation reliability of the power transmission and distribution system. On the other hand, tranquillity is very important in some situations, so the noise generated by the vibration is the key indicator. For example, in the ship power systems, noise will reduce the concealment and safety of ship; while in the EV, noise will influence comfortableness of EV. Most of vibrations have been regarded as an intractable problem. If not handled properly,

Manuscript received 23 May 2023; revised 18 August 2023 and 13 October 2023; accepted 12 November 2023. Date of publication 28 November 2023; date of current version 22 December 2023. This work was supported in part by the National Natural Science Foundation of China (NSFC) under Grant 52077088. Recommended for publication by Associate Editor J. Acero. *(Corresponding author: Zicheng Liu.)*

The authors are with the Huazhong University of Science and Technology, Wuhan 430074, China (e-mail: jiangd@hust.edu.cn; m202171891@hust.edu.cn; liuzc@hust.edu.cn; wangpengye@hust.edu.cn; m201971299@alumni.hust.edu.cn; d202280735@hust.edu.cn; d201277335@alumni.hust.edu.cn; ronghaiqu@hust.edu.cn).

Color versions of one or more figures in this article are available at https://doi.org/10.1109/TPEL.2023.3336954.

Digital Object Identifier 10.1109/TPEL.2023.3336954

they will not only generate unnecessary noise and waste energy, but also cause unexpected damage.

At present, the research on vibration of medium and high-frequency PET is still in its infancy, and the existing literature related to this topic is rare. The vibration and noise of PET and traditional power frequency transformer are the same in principle. The causes of vibration mainly include three aspects: magnetic core vibration, winding vibration, and cooling device vibration [11], [12]. For PET, the vibration of its core is a major concern. Studies in literature [13], [14] point out that the electromagnetic vibration of PET body is caused by three internal electromagnetic excitation forces, namely magnetostrictive force, Maxwell force, and Lorentz force, without considering the vibration of auxiliary cooling equipment such as fan and oil pump. The mechanism of vibration generation and its influencing factors of the PET are analyzed in [15]. The relationship between the vibration acceleration of the iron core and the current and voltage harmonics is quantitatively described. In literature [16], the contribution of Lorentz force is generally considered to be less significant than the other two sources. Both magnetostrictive force and Maxwell force are assumed to be more pronounced sources of vibration source associated with PETs. Based on the magnetostrictive characteristics of toroidal magnetic cores, a new method for calculating transformer vibration of amorphous and nanocrystalline materials is proposed in literature [17]. The current research mainly focuses on the vibration principle analysis of PET. There is a lack of effective vibration reduction strategies.

Moreover, in addition to PET's vibration, the operation of DAB also needs to take other electrical properties into account, such as current stress, reflow power, and so on. These goals often clash with each other. In general, when a design involves numerous conflicting objectives, it is impossible to minimize all of them simultaneously. The use of multiobjective functions has become frequent [18], [19]. When more than one mutually exclusive objective are simultaneously considered, the problem presents a set of solutions called Pareto Front, which includes the optimal solution of each individual objective and also solutions representing the best compromise satisfying all objectives [18], [20].

Besides the regular optimization method, the artificial intelligence provides an entire new approach for the optimization of vibration as well as other performance in power electronics converters. Back propagation neural network (BPNN) consists of various layers such as the input layer, hidden layer, and output layer, and can elucidate the nonlinear mapping relationship between inputs and outputs without giving the specific mathematical equation [21]. In the problem of radiated emission from electric motor, BPNN is used to compute the nonlinear geometrical characteristics of reduced wires model [22]. In a wireless power transfer system, BPNN method is to construct the nonlinear mapping relationship between the impedance of the equivalent load seen by the transmitter and the optimal matched capacitor set [23]. Since the vibration of PET is essentially the result of the strong coupling of electric, magnetic, and mechanical fields, which has a high degree of nonlinearity. We use BPNN to fit the nonlinear mapping relationship between vibration amplitude and electrical parameters of PET in this article.

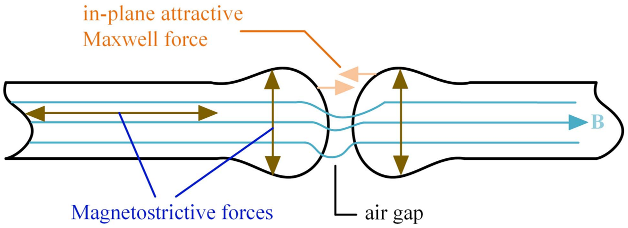

Fig. 2. Mechanisms of Maxwell force and magnetostrictive force at the joint of the core.

1) From the mechanism of vibration generation of PET, the relationship between the internal and external phase shift angles of DAB and the voltage and current of PET is analyzed, and a BPNN with double hidden layer is proposed to predict the vibration. Based on this neural network, the optimized setting of phase-shift angles with minimum vibration are found in the TPS mode, and is then compared against single phase-shift control (SPS), extended phase-shift control (EPS), and double phase-shift control (DPS) under the same transmission power level.
2) The BPNN for vibration prediction is embedded in the nondominated sorting genetic algorithm II (BP-NSGA-II). The current stress, reflow power, along with the vibration of PET were adopted as the target (fitness) function to obtain the Pareto Front. The representative individuals from the Pareto front were analyzed and compared with the minimum vibration solution obtained above.
3) A test platform of transformer vibration based on DAB topology was established, and the feasibility of the above method was verified by experiments.

II. VIBRATION MECHANISM OF PETs

In PETs, the structural vibrations are excited by three types of electromagnetic forces: Maxwell force, magnetostrictive force, and Lorentz force [13], [14].

The Maxwell force is acting on the boundaries (surfaces) between two magnetic media with different magnetic properties (reluctivity), which is typically associated with the air gap regions and the joints of cores in transformers.

The magnetostrictive force is caused by magnetostriction, which represents the deformation of magnetic materials under the effect of magnetic field. For the core materials used for transformer design, the major deformations are due to the Joule magnetostriction [7]. This effect is anisotropic and causes an elongation or contraction of the lamination sheets in the direction of the applied magnetic field, as shown in Fig. 2.

The Lorentz force is acting on the current-conducting windings. It is caused by the electromotive force on the conductor generated by the leakage magnetic field inside the transformer. Since the winding is connected to the transformer core, the vibration of the winding will be coupled to the vibration of the core. In literature [16], the contribution of Lorentz force is usually considered to be less significant than the other two sources. Both magnetostrictive force and Maxwell force are assumed to be more pronounced sources of vibration source

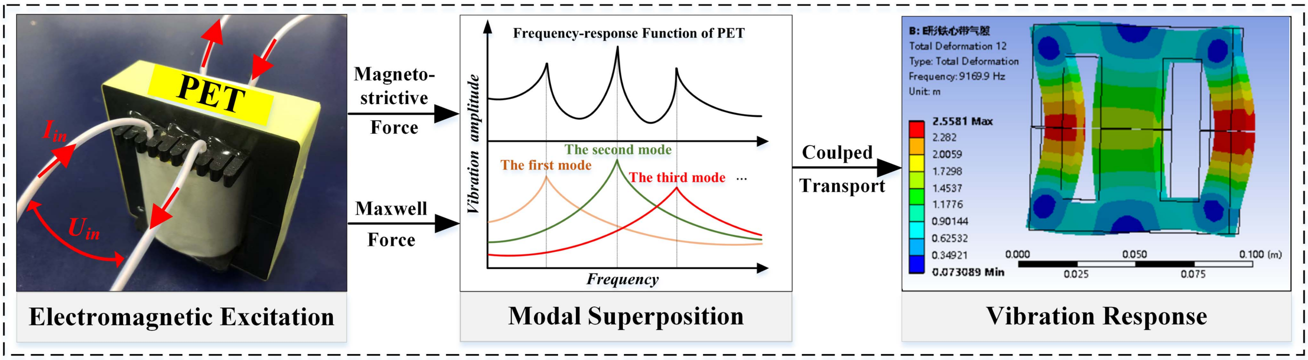

Fig. 3. Mechanism of electromagnetic vibration generation.

Therefore, the magnetostrictive forces and Maxwell forces are the main forces of concern when we study the vibration of PET. By considering the third voltage harmonics, the vibration acceleration of the transformer core caused by magnetostriction can be obtained as follows:

$$a=\frac{v}{t}=\frac{d^2(\Delta L)}{dt^2}$$
$$=-\frac{\lambda_S L}{B_S^2}\begin{bmatrix}2\omega_1^2B_1^2\cos 2\omega_1 t+2\omega_3^2B_3^2\cos(2\omega_3 t+2\theta)\\ +B_1B_3(\omega_1+\omega_3)^2\cos(\omega_1 t+\omega_3 t+\theta)\\ +B_1B_3(\omega_1-\omega_3)^2\cos(\omega_3 t-\omega_1 t-\theta)\end{bmatrix} \tag{1}$$

where λ_S is the coefficient of saturation magnetostriction of the material, L is the length of the material, B_S is the saturation magnetic induction strength of the core (T). Thus, in the case of considering only the third harmonic, the vibration of transformer core includes two times of the fundamental frequency, two times of third harmonic frequency, and the sum and difference of the third harmonic and fundamental frequencies. Similarly, when the number of harmonics increases, the frequency component of magnetostrictive vibration and the corresponding harmonic frequency also meet the correlation of the above formula.

The magnetic force can be expressed as follows:

$$T_n=\frac{B_n^2}{2\mu_0}\propto I(t)^2$$
$$=\sum_{i=1}^{n}\sum_{j=1}^{n}\hat{I}_i\cos(w_i t+\varphi_i)\,\hat{I}_j\cos(w_j t+\varphi_j)$$
$$=\sum_{i=1}^{n}\sum_{j=1}^{n}\frac{1}{2}\hat{I}_i\hat{I}_j\{\cos[(w_i+w_j)t+(\varphi_i+\varphi_j)]$$
$$+\cos[(w_i-w_j)t+(\varphi_i-\varphi_j)]\} \tag{2}$$

where B_n is the normal flux density at the interface, μ_0 is the vacuum permeability, I_i and I_j are the amplitude of the harmonic current, w_i and w_j are the angular frequency of the harmonic current, φ_i and φ_j are the phase of the harmonic current. Consistent with the magnetostrictive force, the vibration frequency component caused by the Maxwell force correlates with the corresponding harmonic current. Since the magnitude of both Maxwell force and magnetostriction are proportional to the square of flux density, the fundamental harmonic of vibration is twice of the excitation frequency. Furthermore, in the presence of harmonics, vibration will also occur at the sum and difference frequencies of the fundamental and the harmonics. Therefore, the vibration of PET will be generated at even times of the excitation frequency, and it is closely related to the fundamental and harmonic of the voltage and current.

In PETs, the electromagnetic excitation passes through various modes of the transformer, and the vibration generated on different effective modes is linearly superimposed to generating the total vibration, as shown in Fig. 3.

1) In the electromagnetic field, the exciting force is mainly produced by two electromagnetic forces, which are Maxwell force and magnetostrictive force. The contribution of these two electromagnetic forces to vibration is not a linear superposition on the amplitude, but a vector addition on the three-dimensional space. In addition, according to the analysis in Section II, these two electromagnetic forces are affected by different electrical parameters. Therefore, it is difficult to suppress the vibration precisely in electromagnetic field.
2) In the mechanical field, the frequency-response function of PET is complex and nonlinear. When the structural system is stimulated by extrinsic motivation to produce motion, it will naturally vibrate at a specific frequency, which is called the modal frequency of the structure. Usually, a transformer has many modal frequencies.

The middle figure in Fig. 3 shows a typical mechanical transfer function curve of PET. Decomposing the mechanical transfer function, the mechanical transfer function curve of each order modal can be obtained. The v-order transfer function in Fig. 3 can be expressed as follows:

$$H(v,\omega)=\frac{1}{\left[\left(\frac{\omega}{\omega_v}\right)^2-1\right]+2\zeta_v\frac{\omega}{\omega_v}i}=|H(v,\omega)|\,e^{j\theta_{v,\omega}} \tag{3}$$

where ω_v and ζ_v are the natural frequency and damping ratio of the ν-order modal, respectively. Obviously the response generated by the excitation force at a certain frequency is the superposition of the response generated on the various modes of

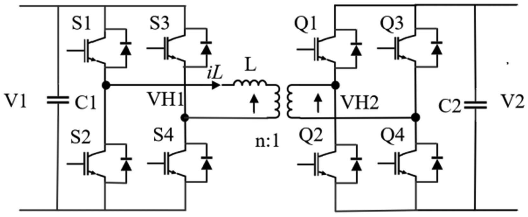

Fig. 4. DAB topology.

PET, which can be expressed as follows:

$$H(\omega) = \sum_{v} H(v, \omega). \tag{4}$$

Due to the two reasons above, the vibration of PET is essentially the result of the strong coupling of electric, magnetic and mechanical fields, which has a high degree of nonlinearity. Since artificial intelligence methods can effectively deal with nonlinear problems, we can apply it to predict and then suppress the vibration.

III. ELECTRICAL CHARACTERISTICS OF DAB UNDER TPS MODULATION

The excitation topology adopted in this article is DAB converter as shown in Fig. 4.

Phase-shift modulation is the main modulation method used in DAB converter. Under phase-shift modulation, the switching signals added to the switching devices on both sides of the H-bridge are square wave signals with the same period and duty ratio of 50%. The switching signals of switching devices on two bridge arms are complementary, and the switching signals of the diagonal switching devices on each side of the H-bridge are consistent. There are phase differences in the switching signals of the diagonal switching devices on the same side (in the bridge) or the corresponding switching devices on both sides (between bridges). The inner phase-shift angles of the original side and the secondary side were defined as D1 and D2, and the outer phase-shift angle between the original side and the secondary side was defined as D3. According to the number of phase-shift variables, phase-shift modulation is mainly divided into SPS control [24], EPS control [25], DPS control [26], and triple phase-shift (TPS) control [27]. TPS has three variables, which could cover the three former control strategies. In other words, the SPS, EPS, and DPS can be regarded as special cases of TPS. Therefore, we concentrated on TPS modulation and its optimization in this article.

According to the size relationship of D1, D2, and D3, TPS is divided into six operating modes in literature [28]. Studies in literature [29] show that modes 2, 3, and 6 will generate larger current on the inductance, which is not only unfavorable to the operation of the converter, but also causing additional loss. The converter should avoid operating in modes 2, 3, 6. Only TPS modes 1, 4, and 5 are discussed here. The waveform of three operating modes is shown in Fig. 5.

TABLE I
POWER TRANSMISSION MODEL OF TPS

Model Classification	**Transmission Power Model**
Mode 1	$P_{1N} = \frac{nU_2}{4fL}(2D_3 - 2D_3{}^2 + 2D_1D_3 - 2D_2D_3 - D_1 - D_1{}^2 + D_1D_2 + D_2 - D_2{}^2)$
Mode 4	$P_{4N} = \frac{nU_2}{4fL}(2D_3 - 2D_1D_3 - D_1 + D_1{}^2 + D_2 - D_1D_2)$
Mode 5	$P_{5N} = \frac{nU_2}{4fL}(2D_3 - D_3{}^2 - 2D_2D_3 - D_1 + D_2 + D_1D_2 - D_2{}^2)$

Among them, the constraint relation of three phase-shift angles under three modes is shown in the following:

$$\begin{aligned} &\text{Mode1}: 0 \le D_1 \le D_3 \le D_2 + D_3 \le 1 \\ &\text{Mode4}: 0 \le D_3 \le D_2 + D_3 \le D_1 \le 1 \\ &\text{Mode5}: 0 \le D_3 \le D_1 \le D_2 + D_3 \le 1. \end{aligned} \tag{5}$$

The transmitted power of the three operating modes is shown in Table I.

During the operation of the DAB converter, the energy stored in the inductor is returned to the power supply when the inductor voltage is positive and the current flowing through the inductor is negative. This stage is known as the reflow stage, which is expressed in (6) as the per-unit representation of the reflow power

$$Q_{TPS} = \begin{cases} \frac{[k(1-D_1)+2D_3-2D_1+D_2-1]^2}{2k+2}, \text{mode 1} \\ \frac{[1+2D_3+(k-2)D_1+D_2-k]^2}{2k-2}, \text{mode 4} \\ \frac{[k(1-D_1)+D_2-1]^2}{2k}, \text{mode 5} \end{cases} \tag{6}$$

where $k = U_{\text{in}}/nU_{\text{out}}$. Additionally, the peak per-unit expression of the inductor current in the three modes is presented in the following:

$$i_{\text{TPS}} = k + 2D_3 - kD_1 + D_2 - 1. \tag{7}$$

Take the DAB topological structure of the phase-shifting inductor on the primary side as an example, the voltage of the primary side of PET after FFT transformation is shown in the following:

$$U = \sum_{n=1,3,5\ldots}^{\infty} \frac{4U_{in}}{n\pi} \sqrt{\frac{1}{2}\left[1+\cos\left(nD_2\pi\right)\right]} \times \sin\left(nw_0t+\varphi\right). \tag{8}$$

As shown in (8), the voltage harmonic content is related to D2. Similarly, the harmonic content of the current is affected by the three phase-shift angles. Therefore, the content of current and voltage harmonics is greatly affected by three phase-shift angles under different modes. Meanwhile, the current and voltage harmonics relate directly to the vibration of PET.

The above analysis reveals that the phase-shift angles can be adjusted to change the voltage and current harmonics of PET, thus suppressing the vibration of PET. The complex nonlinear problem spurs us to seek the neural network for help, which is to find the optimized phase-shift angle corresponding to the minimum vibration.

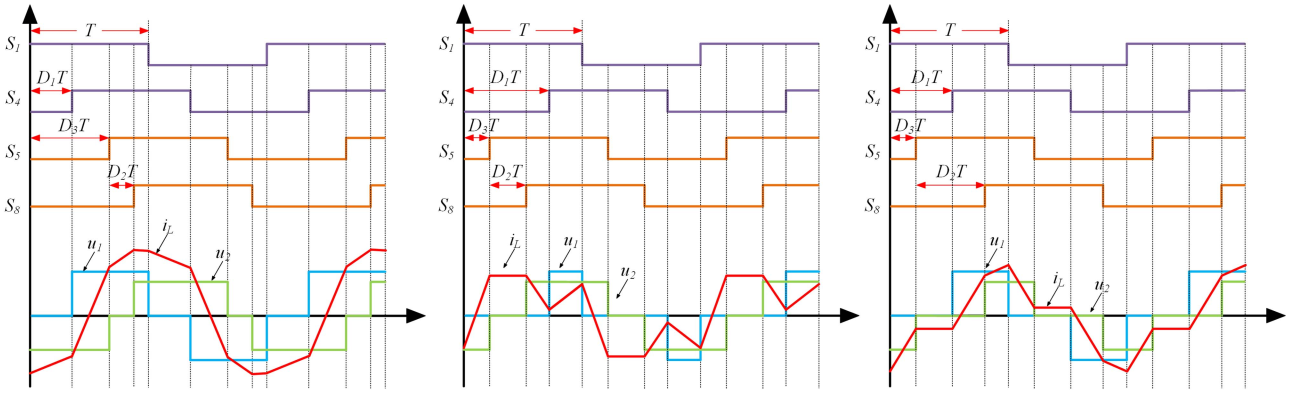

(a) (b) (c)

Fig. 5. Waveform of three operating modes. (a) Mode 1. (b) Mode 4. (c) Mode 5.

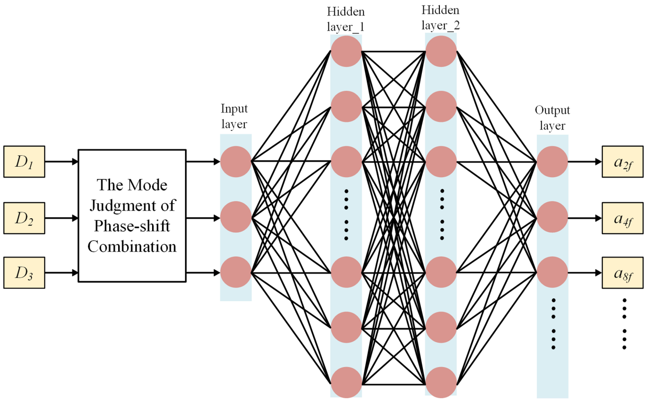

Fig. 6. Proposed BP neural network.

IV. ARTIFICIAL INTELLIGENCE-BASED OPTIMIZATION ALGORITHM

A. BP Neural Network for Vibration Prediction

The structure of BPNN proposed in this article is shown in Fig. 6. The training process of BPNN mainly consists of two processes: forward propagation and error correction in reverse.

According to II, the vibration of PET is affected by voltage harmonics and current harmonics, while according to III, the current components of different control modes of TPS differ greatly. Therefore, mode judgment should be carried out when vibration prediction is made. Under the condition that the transmission power and ambient temperature are consistent, the vibration of PET under different combinations of phase-shift angle are measured. The three phase-shift angles of DAB serve as the input of neural network. The vibration of even multiples of switching frequency serve as the fitting output of the neural network, which are extracted from the measured vibration data. After the mode judgment of different combination of phase-shift angle, vibration fitting is carried out by BPNN.

In the construction of neural network, the selection of the number of hidden layers and the number of neurons in each layer is extremely important. The wrong selection will lead to nonconvergence or overfitting of the network. Single-layer neural networks can only be used for linear separation functions. Multiple hidden layers can be used to fit nonlinear problems. The specific number of hidden layers and neurons will be explained in Section V.

The dataset collected in the experiment is used to train the BPNN. We employed a genetic algorithm with BPNN (BPNN-GA) embedded in separately to find the minimum vibration point, which is shown in Fig. 7. At the same transmission power level, all the combination of phase-shift angles that meet the constraints are calculated and successively replaced into the trained neural network as input. The output of the neural network is compared and the minimum value is found, which corresponds to the optimal phase-shift angles in regards of PET's vibration.

B. BP-NSGA-II

In Section V, it can be observed that as the vibration amplitude decreased, the electrical performance of DAB was compromised, leading to an increase in current stress and reflow power. Hence, when choosing the phase-shift angles, multiple parameters need to be considered comprehensively. This article aims to optimize the vibration amplitude at the key frequency of PET, the current stress on the phase-shifting inductor, and reflow power for DAB. Due to the mutually exclusive relationship between the optimization objectives, it is impossible to attain the optimum solution on all of them. Moreover, assigning clear weights to each objective function is difficult due to the imprecise nature of human thinking. NSGA-II proves to be a suitable multiobjective evolutionary algorithm as it not only has low computational complexity but also eliminates the need for weight coefficients and guarantees excellent protection of individuals. In this study, the NSGA-II algorithm integrates the vibration prediction BP neural network, which is named BP-NSGA-II, was employed to perform the multi-objective optimization of DAB and formulate the Pareto Front. The optimization process is shown in Fig. 8.

In the context of BP-NSGA-II, the quality of a solution is defined according to the dominance criterion. This criterion states that for two solutions $x_1$and x_2, the solution x_1 dominates $x_2$if x_1 is better than or equal to x_2 in all objectives and better than x_2 in at least one of the objectives. Thus, the best solutions

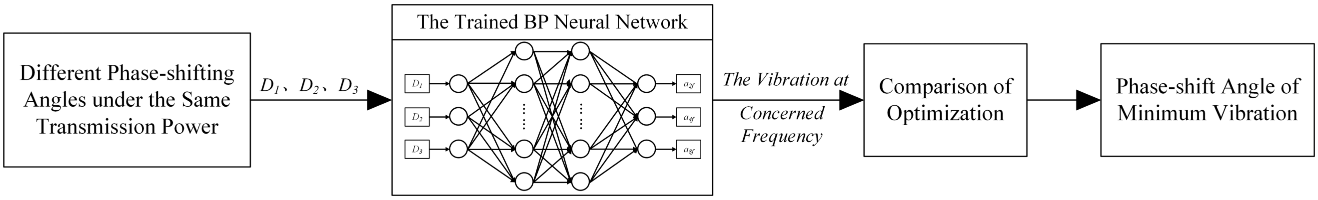

Fig. 7. Process of optimization by using the trained BP neural network.

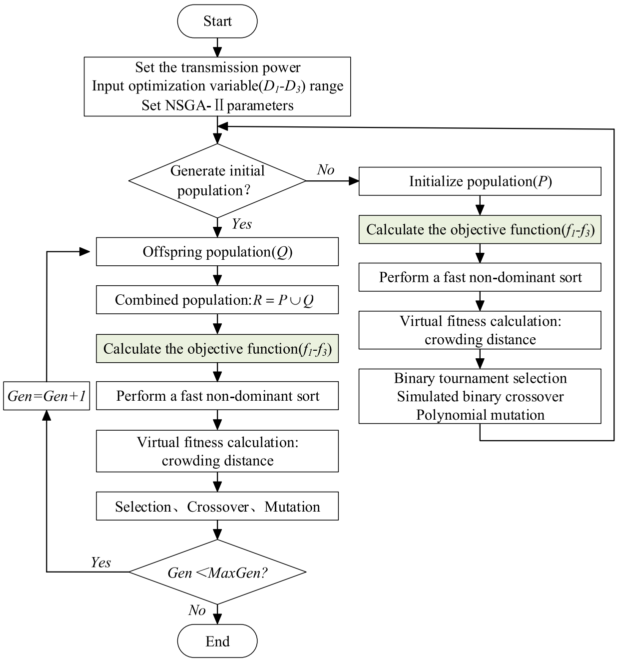

Fig. 8. Flowchart of the DAB optimization.

that are not dominated by any other solution will form the Pareto Front. Furthermore, when all the objectives are simultaneously considered, all solutions along the Pareto Front are equally optimal. Consequently, the problem has several optimal solutions.

As mentioned above, the goal of the described optimization problem is to ensure that the vibration amplitude at the critical frequency of PET is also minimized while the current stress and reflow power are as small as possible at the same power. The optimization objective function is established as follows:

$$\begin{cases} \text{Minimize } Q = f_1\left(D_1, D_2, D_3\right) \\ \text{Minimize } I = f_2\left(D_1, D_2, D_3\right) \\ \text{Minimize } a = f_3\left(D_1, D_2, D_3\right). \end{cases} \tag{9}$$

The constraints are as follows:

$$\begin{cases} P = P_{\text{set}} \\ 0 \leq D_1 \leq 1 \\ 0 \leq D_2 \leq 1 \\ 0 \leq D_3 \leq 1 \end{cases} \tag{10}$$

where $f_1(D_1, D_2, D_3)$ is the function of the reflow power, as shown in (4), $f_2(D_1, D_2, D_3)$ is the function of the current stress, as shown in (5). The trained BPNN was used as $f_3(D_1, D_2, D_3)$ to input three phase shift angles to obtain the predicted PET vibration amplitude, and the obtained vibration predicted value was used as the vibration optimization target. The three objective functions are shown in in Fig. 9.

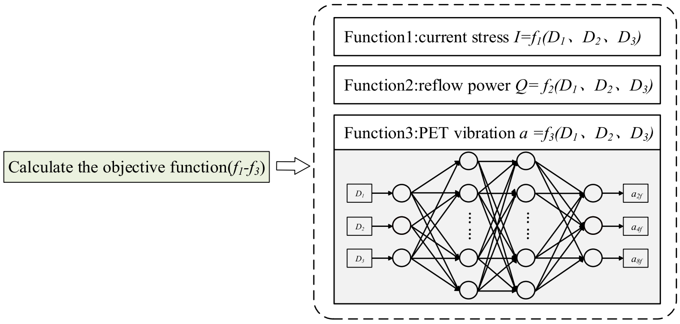

Fig. 9. Composition of the objective function.

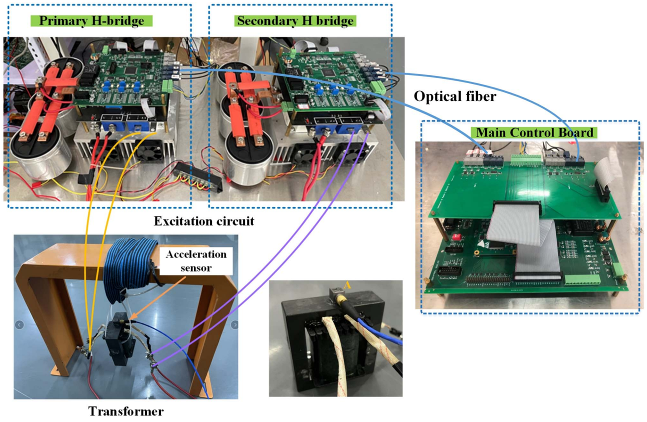

Fig. 10. DAB experimental platform.

V. EXPERIMENTAL RESULT

A. Experimental Setup

The hardware platform built in this experiment include the ferrite transformer with turn ratio $n = 1$, the power electronic excitation circuit, acceleration sensors for vibration test, and the data acquisition cabinet as shown in Fig. 10. The core of PET is solid ferrite. The vibration signal analysis software is LMS Test. Lab. The point A is in the middle of the top of the core and arranged with an acceleration sensor PCB356A44, which has a sensitivity of 50 mV/g (±10%). Its measurement

TABLE II
PARAMETERS OF DAB

Parameter	Value	Parameter	Value
f / Hz	2000	L_r / mH	0.8
P / W	120	R_L / Ω	30
n	1:1	U_{dc} / V	60

range is 0.4 to 10 000 Hz, including the frequency range we are interested in. Each measuring point transmits the vibration signal to the data acquisition instrument through the data cable. The free vibration test method commonly used in vibration measurement is adopted in this article, so we can evaluate the vibration performance more comprehensively. The transformer is suspended with elastic ropes, which is intended to exclude other factors on the modes of transformer. The parameters of the experimental platform are shown in Table II.

In order to fairly evaluate the vibration of transformer core under different phase-shift angles, the same transmission power of PET under different phase-shift angles is guaranteed. For the difference of temperature will affect the modal frequency of ferrite and bring the change of vibration, it is necessary to ensure that the experimental temperature remains almost the same under the same power rating. In the specific vibration test experiment, we used a surface mount temperature sensor UT320D to maintain the temperature of the PET's core at 50 °C ± 1 °C, which is also the thermal equilibrium core temperature at this power.

B. *Experimental Results of BPNN*

We collected the data under mode1, mode4 and mode5 on the DAB platform to verify the generalization capability of the method under different control methods. The phase-shift angle of 500 groups are calculated at the equal transmission power, of which 175 groups belong to mode 1, 175 groups belong to mode 5, and 150 groups belong to mode 4. Due to the influence of transmission power formula and constraint conditions, the range of phase-shift angles of mode 4 is smaller at the same resolution. So the number of data sets used for training of mode 4 is less than the other two modes. On the DAB platform, the three-direction vibration amplitude of point A is measured. The root mean square value of vibration amplitude in *x, y,* and *z* directions is calculated as the total vibration value. In order to ensure the accuracy and generalization ability of the neural network, the ratio of training set to test set is 7:3. The composition of data set is shown in Fig. 11. The learning rate is 0.0001, and the activation function is hyperbolic tangent function tanh, which increases the convergence rate compared with Sigmoid function. The loss is calculated by MES.

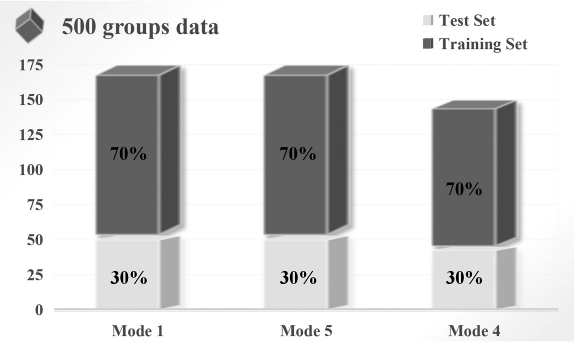

Fig. 11. Composition of dataset.

TABLE III
OFFLINE FITTING TRAINING RESULTS

Model Classification	Accuracy on the training set	Accuracy on the test set
Mode 1	100%	99.09%
Mode 4	100%	99.68%
Mode 5	100%	99.80%

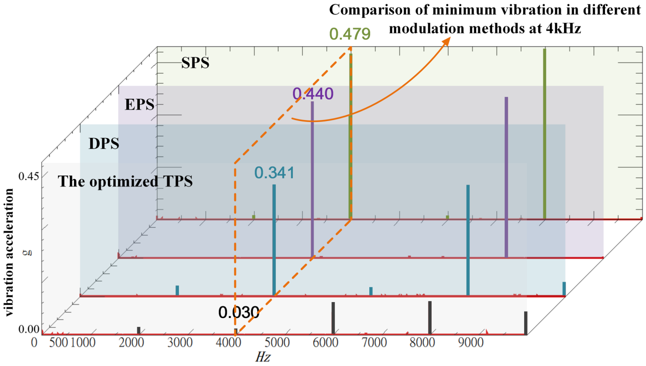

Fig. 12. Comparison of experimental results of the optimized phase-shift angle, SPS, EPS, and DPS.

It is usually sufficient to use the same number of neurons for all hidden layers. According to experience and debugging, the number of hidden layers is determined to be 2, and the number of neurons in each layer is 21. The offline training results are shown in Table III.

The experimental results from the three modes of TPS show that the network used can be applied to the vibration fitting at the key frequency of PET, with good accuracy and generalization ability.

By optimizing the minimum vibration of concerned frequency, we can find the best combination of phase-shift angles under three modes with the same transmission power. Compared with SPS, EPS, and DPS commonly used at this power, the vibration amplitudes at key frequencies under this phase-shift angle are respectively reduced by 24.06, 23.32, and 21.11 dB, as shown in Fig. 12. It can be seen that under this combination of phase-shift angle, except for the minimum vibration amplitude at 4 kHz, the vibration amplitude of other even times frequencies is also relatively small. The electrical experimental waveforms are shown in Fig. 13.

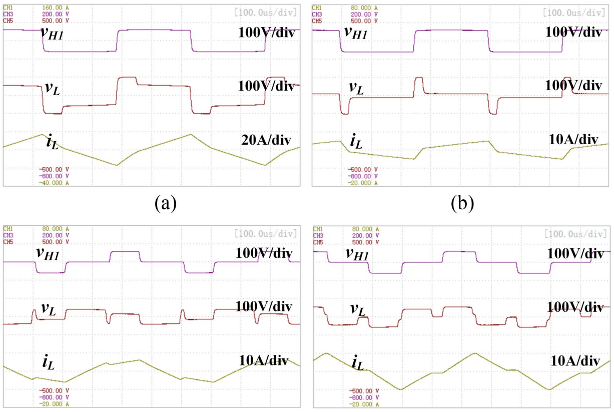

(a) (b)

(c) (d)

Fig. 13. Experimental waveforms of $v_{H1}/v_L/i_L$ of the optimized phase-shift angle, SPS, EPS, and DPS. (a) Optimized TPS. (b) SPS. (c) EPS. (d) DPS.

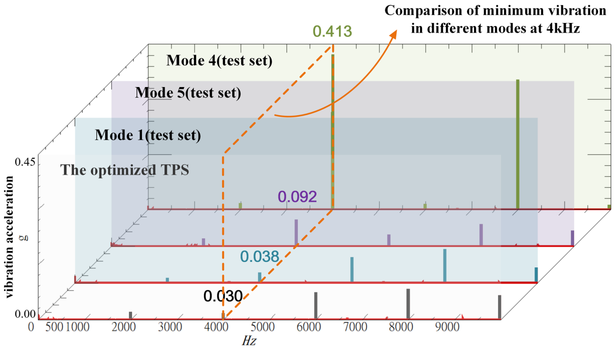

Fig. 14. Comparison of experimental results of the optimized phase-shift angle, mode 1, mode 4, and mode 5.

To further validates the generalization ability of the BPNN, we have compared the experimental results of the optimized TPS mode and standard TPS modes 1, 4, and 5 in Fig. 14. The optimized TPS mode from BP network yields the minimum vibration level of 0.03 g at 4 kHz, which is less than 0.038, 0.092, 0.413 g under three standard TPS modes. This reveals that the BP network succeeds in figuring out a new setting of phase-shift angles, which is better than all the training data in regards of vibration performance. Moreover, Fig. 15 demonstrates that the optimized TPS mode leads to different voltage and current waveforms from all the other three standard TPS modes, which is the essential reason for vibration reduction.

C. Comparison Analysis of Different Hidden Layers

In order to demonstrate the rationality of the number of hidden layers, the architecture adopted in the experiment was compared with the neural network with different hidden layers and the same total number of neurons. Taking the neural network of mode 5 as an example, the training accuracy and training time of each neural network are shown in Table IV.

From Table IV, compared with the double-hidden layer architecture, the accuracy of the single-layer neural network decreases by 26.65% and the vibration value cannot be well fitted, while the number of iterations of the three-layer neural network increases and the training time is longer. Therefore, it is reasonable to use a neural network architecture with double hidden layers.

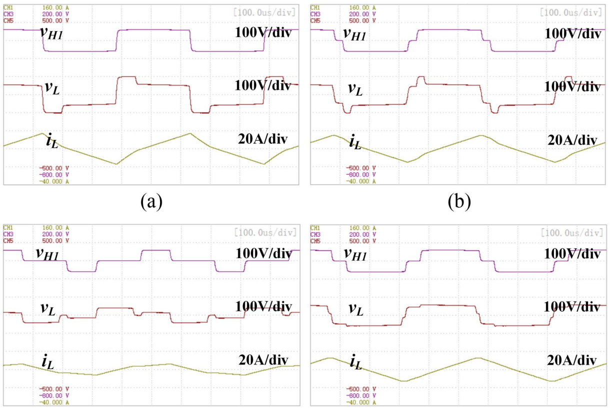

(a) (b)

(c) (d)

Fig. 15. Experimental waveforms of $v_{H1}/v_L/i_L$ of the optimized phase-shift angle, mode 1, mode 4, and mode 5. (a) Optimized TPS. (b) Mode 1. (c) Mode 5. (d) Mode 4.

TABLE IV
COMPARISON RESULTS FOR DIFFERENT NUMBERS OF HIDDEN LAYERS

The number of hidden layers	**1**	**2**	**3**
Accuracy on the training set	73.35%	100%	100%
Accuracy on the test set	68.63%	99.80%	97.32%
The training time consumed	38.57s	41.40s	58.08s

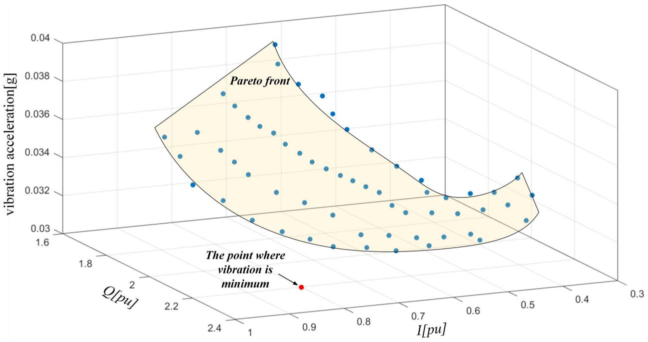

Fig. 16. Pareto front of BP-NSGA-II.

D. Experimental Results of BP-NSGA-II

The BP-NSGA-II algorithm in this article uses the following parameters.

1) Population size: $n_{pop} = 60$ individuals.
2) Maximum number of generations: 100.
3) The mutation rate is 30%. The remaining individuals are obtained by recombination.
4) Individuals differing in at least one gene.

After 100 generations the iterative process found the solutions depicted in Fig. 16. The yellow surface represents the Pareto

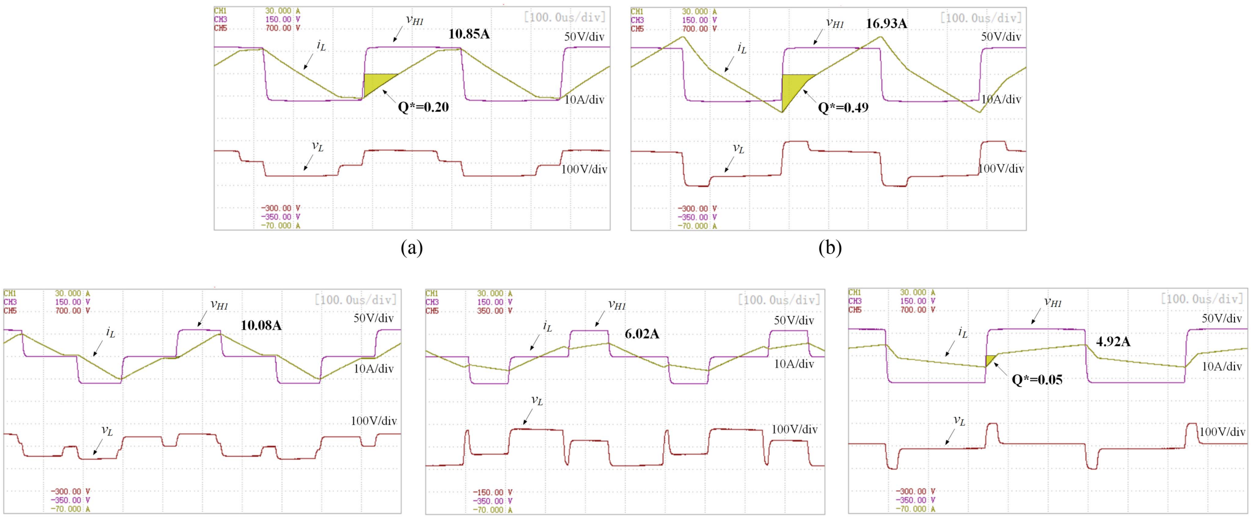

(a) (b)

(c) (d) (e)

Fig. 17. Comparison of experimental waveforms of the (a) BP-NSGA-II, (b) BPNN-GA, (c) DPS, (d) EPS, and (e) SPS.

TABLE V
COMPARISON RESULTS OF FIVE CONDITIONS

The Modulation Method	Vibration	Reflow Power[pu]	Current Stress
The representative individual from BP-NSGA-II	0.033g	0.20	10.85A
BPNN-GA	0.030g	0.49	16.93A
SPS	0.479g	0.05	4.92A
EPS	0.440g	0	6.02A
DPS	0.341g	0.004	10.08A

front and indicates that the BP-NSGA-II algorithm achieves high levels of distribution and convergence. The optimized TPS mode found by the BP neural network in Section V-B is denoted by the red point. It can be seen that although the vibration of PET is the smallest, the current stress and reflow power are at a high level, which is not conducive to the operation of DAB.

To evaluate the proposed BP-NSGA-II algorithm comprehensively, one representative individual on the Pareto front was selected, and then compared with common SPS, EPS, DPS, and the optimized TPS using BPNN-GA based on three dimensions of current stress, reflow power and PET's vibration. Fig. 17 displays experimental waveforms for each of the five operating conditions. The parameters of the three dimensions are listed in Table V.

We have employed a 3-point scoring system ranging from 0 (lowest performance) to 3 (highest performance), and drew a radar chart as shown in Fig. 18. Key findings are summarized below:

1) PET exhibited obvious vibration under SPS, EPS, and DPS.
2) Utilizing BPNN-GA to optimize the working condition can effectively reduce PET vibration but worsen other electrical properties of DAB, such as current stress and reflow power.
3) Compared with BPNN-GA, the vibration amplitude of BP-NSGA-II increased from 0.030 to 0.033 g, resulting in an increase of 0.82 dB. However, even after this increase, the vibration remained at a very low level. Additionally, the current stress and reflow power decreased by 35.9% and 59.2%, respectively. The optimal solution achieved by BP-NSGA-II not only maintains the low level of vibration

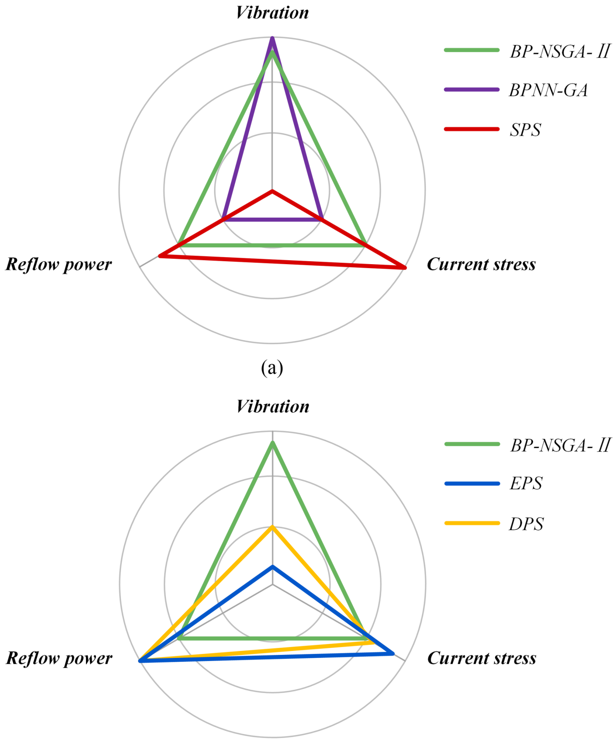

(a)

(b)

Fig. 18. Radar chart of five modulations.

amplitude in PET but also partially optimizes its electrical performance.

In the above comparison, the representative individual is selected on the Pareto front with relatively small vibration. In actual operation, different phase-shift angles on Pareto front can be selected according to the different emphasis on the objective function, which has guiding significance for the parameter selection of DAB operation.

VI. CONCLUSION

This article focuses on vibration suppression of PET and multiobjective optimization of DAB's operation. First, it reviews the mechanism of vibration generation of PET and analyzes the characteristics of voltage and current waveforms of PET under different TPS modes. Then the BPNN with double hidden layers and one mode judgment layer is proposed to fit this nonlinear problem. Furthermore, based on the trained neural network, we found the optimized phase-shift angle with minimum vibration in the TPS mode. The experimental results show that compared with the common SPS, EPS, and DPS under the same transmission power level, the vibration amplitude under the optimized mode is reduced by 24.06, 23.32, and 21.11 dB, respectively. The proposed data-driven fitting method provides a new perspective for the future study of PET's vibration.

Second, this article introduces a multiobjective method to optimize DAB based on BP-NSGA-II. A comparative analysis shows that the operation parameters following multiobjective optimization maintain PET vibration at a low level while simultaneously optimizing DAB's operation performance. This method provides guidance for selecting DAB operation parameters when considering both electrical and mechanical performance. Overall, this article offers promising directions for exploiting the artificial intelligence methods to solve multiphysics coupling problems in power electronics.

REFERENCES

[1] W. Jialiang et al., "Analysis of DC grid prospects in China," *Proc. Chin. Soc. Elect. Eng.*, vol. 32, no. 13, pp. 7–12, 2012.

[2] C. Sun, X. Zhang, J. Zhang, M. Zhu, and J. Huang, "Hybrid input-series–output-series modular DC–DC converter constituted by resonant and nonresonant dual active bridge modules," *IEEE Trans. Ind. Electron.*, vol. 69, no. 1, pp. 1062–1069, Jan. 2022.

[3] W. M. Zawieska, *The Active Noise Control Issues Related to the Noise Generated by the Power Transformers*. Kraków, Poland: Mechanics /AGH Univ. Sci. Technol., 2005, pp. 155–161.

[4] Z. Tong, "Review of power electronic transformers based on modular multilevel converters," *Proc. Chin. Soc. Elect. Eng.*, vol. 42, no. 15, pp. 5630–5649, 2022.

[5] Q. Zhaoming, Z. Junming, and S. Kuang, "Status and development of power semiconductor devices and its applications," *Proc. Chin. Soc. Elect. Eng.*, vol. 34, no. 29, pp. 5149–5161, 2014.

[6] L. Zixin, G. Fanqiang, and Z. Cong, "Research review of power electronic transformer technologies," *Proc. Chin. Soc. Elect. Eng.*, vol. 38, no. 5, pp. 1274–1289, 2018.

[7] A. Belahcen, "Magnetoelasticity, magnetic forces and magnetostriction in electrical machines," Ph.D. dissertation, Helsinki Univ. Technol., Espoo, Finland, 2004.

[8] L. Zheng et al., "SiC-based 5-kV universal modular soft-switching solid-state transformer (M-S4T) for medium-voltage DC microgrids and distribution grids," *IEEE Trans. Power Electron.*, vol. 36, no. 10, pp. 11326–11343, Oct. 2021.

[9] Y. Chen, S. Zhao, Z. Li, X. Wei, and Y. Kang, "Modeling and control of the isolated DC–DC modular multilevel converter for electric ship medium voltage direct current power system," *IEEE J. Emerg. Sel. Topics Power Electron.*, vol. 5, no. 1, pp. 124–139, Mar. 2017.

[10] R. T. Naayagi, A. J. Forsyth, and R. Shuttleworth, "High-power bidirectional DC–DC converter for aerospace applications," *IEEE Trans. Power Electron.*, vol. 27, no. 11, pp. 4366–4379, Nov. 2012.

[11] W. M. Zawieska, "A power transformer as a source of noise," *Int. J. Occup. Saf. Ergonom.*, vol. 13, no. 4, pp. 381–389, 2007.

[12] D. Miljkovic, "Active reduction of power transformer noise based on synchronous averaging of the residual noise signal," in *Proc. 35th Int. Conv.*, 2012, pp. 875–880.

[13] P. Shuai and J. Biela, "Influence of material properties and geometric shape of magnetic cores on acoustic noise emission of medium-frequency transformers," *IEEE Trans. Power Electron.*, vol. 32, no. 10, pp. 7916–7931, Oct. 2017.

[14] M. Rossi and J. Le Besnerais, "Vibration reduction of inductors under magnetostrictive and Maxwell forces excitation," *IEEE Trans. Magn.*, vol. 51, no. 12, Dec. 2015, Art. no. 8403406.

[15] D. Jiang, X. Peng, Z. Liu, P. Wang, S. Yan, and R. Qu, "Vibration performance of a power electronic transformer under different phase-shift modulation methods," *IEEE Trans. Ind. Appl.*, vol. 58, no. 6, pp. 7529–7538, Nov./Dec. 2022, doi: 10.1109/TIA.2022.3202763.

[16] P. Shuai and J. Biela, "Investigation of acoustic noise sources in medium frequency, medium voltage transformers," in *Proc. 16th Eur. Conf. Power Electron. Appl.*, 2014, pp. 1–11.

[17] P. Zhang and L. Li, "Vibration and noise characteristics of high-frequency amorphous transformer under sinusoidal and non-sinusoidal voltage excitation," *Int. J. Elect. Power Energy Syst.*, vol. 123, 2020, Art. no. 106298.

[18] M. S. Mohammed and R. A. Vural, "NSGA-II+FEM based loss optimization of three-phase transformer," *IEEE Trans. Ind. Electron.*, vol. 66, no. 9, pp. 7417–7425, Sep. 2019.

[19] L. A. Pereira, S. Haffner, G. Nicol, and T. F. Dias, "Multiobjective optimization of five-phase induction machines based on NSGA-II," *IEEE Trans. Ind. Electron.*, vol. 64, no. 12, pp. 9844–9853, Dec. 2017.

[20] Y. Hua, H. Zhu, M. Gao, and Z. Ji, "Multiobjective optimization design of permanent magnet assisted bearingless synchronous reluctance motor using NSGA-II," *IEEE Trans. Ind. Electron.*, vol. 68, no. 11, pp. 10477–10487, Nov. 2021.

[21] B. Singh and S. R. Arya, "Back-propagation control algorithm for power quality improvement using DSTATCOM," *IEEE Trans. Ind. Electron.*, vol. 61, no. 3, pp. 1204–1212, Mar. 2014.

[22] S. Wei, Z. Pan, J. Yang, and P. Du, "A reduction technique for modeling closely spaced wires considering proximity effects applied to predict radiated emission from electric motor," *IEEE Trans. Ind. Electron.*, vol. 68, no. 12, pp. 12535–12542, Dec. 2021.

[23] Y. Li, W. Dong, Q. Yang, J. Zhao, L. Liu, and S. Feng, "An automatic impedance matching method based on the feedforward-backpropagation neural network for a WPT system," *IEEE Trans. Ind. Electron.*, vol. 66, no. 5, pp. 3963–3972, May 2019.

[24] M. N. Kheraluwala, R. W. Gascoigne, D. M. Divan, and E. D. Baumann, "Performance characterization of a high-power dual active bridge DC-to-DC converter," *IEEE Trans. Ind. Appl.*, vol. 28, no. 6, pp. 1294–1301, Nov./Dec. 1992.

[25] S. S. Shah and S. Bhattacharya, "A simple unified model for generic operation of dual active bridge converter," *IEEE Trans. Ind. Electron.*, vol. 66, no. 5, pp. 3486–3495, May 2019.

[26] H. Bai and C. Mi, "Eliminate reactive power and increase system efficiency of isolated bidirectional dual-active-bridge DC–DC converters using novel dual-phase-shift control," *IEEE Trans. Power Electron.*, vol. 23, no. 6, pp. 2905–2914, Nov. 2008.

[27] K. Wu, C. W. de Silva, and W. G. Dunford, "Stability analysis of isolated bidirectional dual active full-bridge DC–DC converter with triple phase-shift control," *IEEE Trans. Power Electron.*, vol. 27, no. 4, pp. 2007–2017, Apr. 2012.

[28] A. K. Bhattacharjee and I. Batarseh, "Optimum hybrid modulation for improvement of efficiency over wide operating range for triple-phase-shift dual-active-bridge converter," *IEEE Trans. Power Electron.*, vol. 35, no. 5, pp. 4804–4818, May 2020.

[29] X. Ma, A. Tong, B. Li, L. Hang, G. Li, and P. Shen, "ZVS operation of DAB converter based on triple-phase-shift modulation scheme with optimized inductor current," in *Proc. 43rd Annu. Conf. IEEE Ind. Electron. Soc.*, 2017, pp. 4702–4707.

Dong Jiang (Senior Member, IEEE) received the B.S. and M.S. degrees in electrical engineering from Tsinghua University, Beijing, China, in 2005 and 2007, respectively, and the Ph.D. degree in power electronics and motor drives from the University of Tennessee, Knoxville, TN, USA, in 2011.

He was with the United Technologies Research Center, East Hartford, CT, USA, as a Senior Research Scientist/Engineer, from January 2012 to July 2015. He has been with the Huazhong University of Science and Technology, Wuhan, China, as a Professor, since July 2015. His main research interests include power electronics and motor drives, with more than 100 published IEEE journal and conference papers in this area.

Dr. Jiang was the recipient of six best paper awards in IEEE conferences. He is an Associate Editor for IEEE TRANSACTIONS ON INDUSTRY APPLICATIONS and the Chair of IEEE Power Electronics Society Wuhan Chapter.

Shang Gong (Student Member, IEEE) was born in Hubei, China, in 1997. He received the B.S. degree in electrical engineering from the Huazhong University of Science and Technology (HUST), Wuhan, China, in 2019. He is currently working toward the master degree in electrical engineering from the School of Electronic and Electrical Engineering, HUST.

His research interests include control of multiphase machines and vibration performance of power electronic transformer.

Zicheng Liu (Senior Member, IEEE) received the B.S. degree in hydropower engineering from the Huazhong University of Science and Technology (HUST), Wuhan, China, in 2011, and the Ph.D. degree in electrical engineering from Tsinghua University, Beijing, China, in 2016.

From 2014 to 2015, he was a Visiting Student with Purdue University, West Lafayette, IN, USA. From 2016 to 2018, he was a Postdoc Researcher with Beijing Jiaotong University, Beijing, China. He is currently an Associate Professor with HUST. His research interests include multiphase motor control systems and transportation electrification.

Dr. Liu was the recipient of two prize paper awards in IEEE conferences and the second-place prize paper award of IEEE Journal of Emerging and Selected Topics in Power Electronics. He is the Vice Chair of IEEE Power Electronics Society Wuhan Chapter.

Pengye Wang (Graduate Student Member, IEEE) was born in Shandong, China, in 1996. He received the B.S. degree in electrical engineering from the China University of Mining and Technology, Jiangsu, China, in 2019, and the M.S. degree in electrical engineering from the School of Electrical and Electronic Engineering, Huazhong University of Science and Technology, Wuhan, China, in 2022, where he is currently working toward the Ph.D. degree in electrical engineering.

His research interests include inverter topology and multiphase motor control systems.

Xiaokang Peng (Student Member, IEEE) was born in Anhui, China, in 1993. He received the B.S. degree in electrical engineering and automation from the Wuhan University of Technology, Wuhan, China, in 2015, and the M.S. degree in new energy science and engineering from the Huazhong University of Science and Technology, Wuhan, in 2022, and the M.S. degree in new energy science and engineering from Ecole Nationale Supérieure des Mines de Paris, Paris, France, in 2022.

He is currently engaged in electrical design with the Electromechanical & Information Engineering Institute, Anhui Survey & Design Institute of Water Resources & Hydropower Company Ltd. His research interests include multiphase energy conversion in wind power generation, the vibration and noise analysis of the power electronic transformer, and water conservancy & hydropower engineering design.

Rui Li received the Ph.D. degree in electrical engineering from the Huazhong University of Science and Technology, Wuhan, China, in 2014.

He is currently a Senior Engineer with Wuhan Second Ship Design and Research Institute, Wuhan. His research interests include multiphase motor control systems, low noise motor design, and high-efficiency high power density electrical energy conversion.

Jiuqing Cai received the Ph.D. degree in electrical engineering from the Huazhong University of Science and Technology, Wuhan, China, in 2017.

His research interests include ship integrated power system and application of power electronics technology.

Ronghai Qu (Fellow, IEEE) received the B.E. and M.S. degrees in electrical engineering from Tsinghua University, Beijing, China, in 1993 and 1996, respectively, and the Ph.D. degree in electrical engineering from the University of Wisconsin-Madison, Madison, WI, USA, in 2002.

He had been with the General Electric (GE) Global Research Center, Niskayuna, NY, USA, as a Senior Electrical Engineer with the Electrical Machines and Drives Laboratory from 2003 to 2010. From 2012 to 2016, he served as the Deputy Dean of the School of Electrical & Electronic Engineering. He has authored and coauthored more than 400 technical papers including 14 IEEE award papers and holds more than 170 patents. His research interests include design and drive of electrical machines.

Dr. Qu was the recipient of 11 GE GRC awards including EPST Technical Achievement Award, Outstanding Teamwork and Management Award. In 2010 he joined Huazhong University of Science & Technology, Wuhan, China. He is currently the Director of State and Province Joint Engineering Research Center of Novel Electrical Machines, and the Director of the Center for Advanced Electrical Machines and Drives. He is currently a member of ICEM NPO AdCom and the Chair of IEEE Industry Application Society Wuhan Chapter. He is also a winner of several other awards including 2020 Science and Technology Invention Award (1st prize) from China Electrotechnical Society, the 7th Nagamori Awards from Nagamori Foundation, Japan, 2021, and two gold Medals from the 47th Exhibition of Inventions of Geneva, 2019, and the 12th Innovation and Entrepreneurial Figure Award, China Association of Inventions, 2022. He is a Fellow of China Electrotechnical Society.